Membrane-Docking Loops of the cPLA2 C2 Domain: Detailed Structural Analysis of the Protein−Membrane Interface via Site-Directed Spin-Labeling†

Nathan J. Malmberg, David R. Van Buskirk, and Joseph J. Falke*

Department of Chemistry and Biochemistry, University of Colorado, Boulder, Colorado 80309-0215

Received June 30, 2003; Revised Manuscript Received September 4, 2003

ABSTRACT: C2 domains are protein modules found in numerous eukaryotic signaling proteins, where their function is to target the protein to cell membranes in response to a Ca^{2+} signal. Currently, the structure of the interface formed between the protein and the phospholipid bilayer is inaccessible to high-resolution structure determination, but EPR site-directed spin-labeling can provide a detailed medium-resolution view of this interface. To apply this approach to the C2 domain of cytosolic phospholipase A_2 ($cPLA_2$), single cysteines were introduced at all 27 positions in the three Ca^{2+}-binding loops and labeled with a methanethiosulfonate spin-label. Altogether, 24 of the 27 spin-labeled domains retained Ca^{2+}-activated phospholipid binding. EPR spectra of these 24 labeled domains obtained in the presence and absence of Ca^{2+} indicate that Ca^{2+} binding triggers subtle changes in the dynamics of two localized regions within the Ca^{2+}-binding loops: one face of the loop 1 helix and the junction between loops 1 and 2. However, no significant changes in loop structure were detected upon Ca^{2+} binding, nor upon Ca^{2+}-triggered docking to membranes. EPR depth parameters measured in the membrane-docked state allow determination of the penetration depth of each residue with respect to the membrane surface. Analysis of these depth parameters, using an improved, generalizable geometric approach, provides the most accurate picture of penetration depth and angular orientation currently available for a membrane-docked peripheral protein. Finally, the observation that Ca^{2+} binding does not trigger large rearrangements of the membrane-docking loops favors the electrostatic switch model for Ca^{2+} activation and disfavors, or places strong constraints on, the conformational switch model.

Cellular signals are transmitted by a variety of mechanisms, including the release of small molecule second messengers such as Ca^{2+} or phosphoinositides, protein translocation between cellular compartments, and protein posttranslational modification. C2 domains are protein-signaling modules found in numerous signaling proteins (*1*−*11*). Usually, the function of such C2 domains is to trigger the translocation of proteins to specific cellular membranes in response to a Ca^{2+} signal. This targeting increases the likelihood of interaction of the signaling protein with its downstream target, often a membrane-bound lipid or protein.

Cytosolic phospholipase A_2 ($cPLA_2$)[1] hydrolyzes lipids containing arachadonic acid and thereby releases this important precursor from nuclear and endoplasmic reticulum (ER) membranes in response to a Ca^{2+} signal (*12*). The protein consists of two structurally distinct domains, an N-terminal C2 domain, which binds two Ca^{2+} ions and triggers docking to phospholipid membranes, and a C-terminal catalytic domain, which hydrolyzes the sn-2 ester of arachidonic acid-containing phospholipids (*13*). The protein initiates pathways that synthesize prostaglandins and trigger inflammation and that synthesize leukotrienes released as powerful chemoattractants (*14*, *15*).

Previous studies have characterized a number of Ca^{2+}-regulated C2 domains that bind multiple Ca^{2+} ions and trigger docking to phospholipids on the surfaces of cellular membranes (*3*, *7*, *16*−*20*). Most of these domains employ an electrostatic mechanism of docking, and as a result, they require anionic lipids such as phosphatidylserine (PS) for membrane docking. In contrast, the C2 domain of cytosolic phospholipase A_2 ($cPLA_2$) employs a hydrophobic mechanism to dock to membrane surfaces containing neutral phospholipids such as phosphatidylcholine (PC). Since the $cPLA_2$ C2 domain is the first characterized example of a C2 domain that exhibits a hydrophobic docking mechanism, it is known to exhibit novel features of Ca^{2+} activation and membrane docking. These features are likely to be relevant to newly reported C2 and C2-like domains also proposed to use a hydrophobic docking mechanism, such as that of 5-lipoxygenase (*21*).

Three high-resolution structures of the C2 domain of $cPLA_2$ have been solved (*22*−*24*). Two of these structures define the isolated C2 domain in crystals or solution, respectively, while the third reveals the crystal structure of the domain in the context of the full-length protein. These structures have confirmed that the $cPLA_2$ C2 domain, like other structurally characterized C2 domains (*25*−*30*), exhibits the classic eight-strand antiparallel β-sandwich of the C2 motif, with three interstrand Ca^{2+}-binding loops that bind

† Support provided by NIH Grant GM R01-63235 (to J.J.F.).

* To whom correspondence should be addressed. E-mail: falke@colorado.edu. Tel: (303) 492-3503.

[1] Abbreviations: $cPLA_2$, cytosolic phospholipase A_2; PS, phosphatidylserine; PC, phosphatidylcholine; PE, phosphoethanolamine; MTSSL, 1-oxyl-2,2,5,5-tetramethyl-Δ^3-pyrroline-3-methyl methanethiosulfonate; NiEDDA, Ni(II) ethylenediamine diacetic acid.

10.1021/bi035119+ CCC: $25.00
Published on Web 10/22/2003

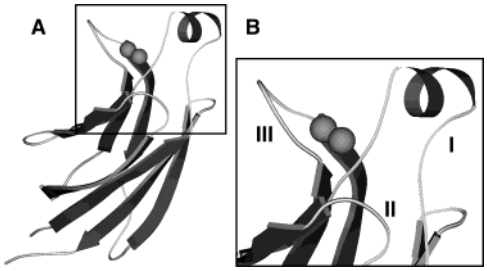

FIGURE 1: Structure of the C2 Domain of $cPLA_2$. (A) The crystal structure of the C2 domain of $cPLA_2$ is shown (*22*), with eight β-strands depicted by ribbons and two Ca^{2+} ions shown as spheres. (B) Enlarged view of the three Ca^{2+}-binding loops (CBLs). Figure was generated in Molscript (*56*).

two Ca^{2+} ions at saturating Ca^{2+} concentrations (Figure 1). Separate equilibrium dialysis and fluorescence binding studies carried out under physiological ionic conditions have revealed that the isolated $cPLA_2$ C2 domain binds two Ca^{2+} ions, both when free in solution and when docked to membranes (*19*). To date, this C2 domain has failed to crystallize in the absence of Ca^{2+} or in the presence of a phospholipid headgroup analogue; thus, crystallographic studies have not yet provided information about the structure of the domain either in the absence of Ca^{2+} or in the presence of lipids. NMR studies have detected Ca^{2+}-triggered chemical shift changes in the Ca^{2+}-binding loops but could not clarify whether these changes reflect a conformational change, a change in the electrostatic environment, or a change in loop dynamics.

Previous NMR, fluorescence, and EPR reports have indicated that the Ca^{2+}-binding loops of the $cPLA_2$ C2 domain provide most or all of the major lipid contacts when the domain docks to membranes. NMR studies have detected protein chemical shift changes localized primarily to the Ca^{2+}-binding loops when the domain docks to the a lipid micelle (*23*). Fluorescence studies utilizing fluorescein probes coupled to engineered single-cysteine residues scattered over the protein surface have revealed direct fluorophore interactions between the Ca^{2+}-binding loops and the membrane and have indicated that other regions of the protein surface do not contact the membrane (*31*). EPR studies using nitroxide spin probes coupled to cysteines scattered over the protein surface have also localized the membrane-binding surface to the Ca^{2+}-binding loops (*32*, *58*) and have defined an initial model for the depth of penetration of the domain into the membrane and its angular orientation relative to the membrane surface (*32*). These previous studies have raised important questions about the nature of the membrane-docking interaction. First, the information provided by scattered fluorescence- and spin-labeling sites could not rule out the possibility that the Ca^{2+}-binding loops undergo major structural rearrangements upon Ca^{2+} binding and membrane docking. Moreover, the precision of the proposed EPR model for penetration depth and angular orientation was limited by the small number of positions examined in the Ca^{2+} and membrane-binding loops (only six out of 27 loop positions were examined (*32*)). The answers to these questions about the Ca^{2+}-binding loops of the $cPLA_2$ C2 domain could have broad implications since the Ca^{2+}-binding loops of other C2 domains also dominate membrane-docking interactions (*33*−*35*).

The present study introduces cysteines into all 27 positions of the three Ca^{2+}-binding loops of the human $cPLA_2$ C2 domain. This cysteine-scanning approach allows coupling of a thiol-specific spin-label to each cysteine for EPR spectroscopy (*36*). For 24 of the 27 positions, EPR spectra have been acquired for the free apo domain, the free Ca^{2+}-occupied domain, and the Ca^{2+}-occupied domain bound to unilamellar phospholipid vesicles composed of a physiological mixture of phosphatidylcholine (PC) and phosphatidylserine (PS). The EPR spectra in the presence and absence of Ca^{2+} indicate that Ca^{2+} binding does not trigger major rearrangements of the Ca^{2+}-binding loops. For the membrane-bound domains, continuous-wave power saturation measurements were used to calculate an EPR depth parameter for each spin-label in the loops. The resulting depth parameters indicate that the conformation of the Ca^{2+}-binding loops docked to membranes is similar to their Ca^{2+}-loaded conformation in the crystal and NMR structures. Finally, a novel and generalizable geometric analysis was applied to the extensive set of EPR depth parameters to more precisely determine the penetration depth and angular orientation of the domain with respect to the membrane surface. Notably, the interaction with the membrane is dramatically different than observed for C2 domains that exhibit an electrostatic docking mechanism.

MATERIALS AND METHODS

Reagents. 1-Palmitoyl-2-oleoyl-glycero-3-phosphocholine (POPC or PC) and 1-palmitoyl-2-oleoyl-glycero-3-phosphoserine (POPS or PS) and 1-palmitoyl-2-stearoyl(*n*-DOXYL)-glycero-3-phosphocholine ($n = 5, 7, 10, 12$) were purchased from Avanti Polar Lipids. *N*-(5-Dimethylaminonaphthalene-1-sulfonyl)-1,2-dihexadecanoyl-*sn*-glycero-3-phosphoethanolamine (dansyl-PE) was purchased from Molecular Probes. 1-Oxyl-2,2,5,5-tetramethyl-Δ^3-pyrroline-3-methyl methanethiosulfonate (MTSSL) was purchased from Toronto Research Chemicals. NiEDDA was synthesized by dissolving 17 mM ethylenediamine diacetic acid (EDDA) and 17 mM $Ni(OH)_2$ (both from Sigma) in water at 60 °C. The clear blue solution was then filtered, lyophilized, resuspended in ethanol, and filtered again to remove unreacted material. Phospholipid membranes were prepared by drying chloroform suspensions of phospholipid mixtures under nitrogen and vortexing to resuspend the dried lipid films in standard assay buffer (20 mM HEPES pH 7.4, 100 mM KCl). Small unilamellar vesicles were prepared by sonication with a Misonix sonicator for 5 min at maximum power (microtip, setting 5) as previously described (*3*, *19*). Large unilamellar vesicles were prepared by extrusion through a 100 nm membrane in a mini-extruder from Avanti Polar Lipids as previously described (*32*, *35*).

Protein Mutagenesis, Expression, and Purification. Single cysteine mutants of the human $cPLA_2$ C2 domain (residues 1−138) were generated using the single-stranded mutagenesis technique of Kunkel et al. as previously described (*31*, *37*). Cysteine mutants were expressed as inclusion bodies in *Escherichia coli*, then were isolated, denatured, refolded, and properly folded protein purified by affinity chromatography as previously described (*32*), except that the buffer used to solubilize the inclusion bodies contained 37 mM MTSSL to label the protein in an unfolded state. The MTSSL

forms a disulfide bond to the cysteine sulfhydryl of the protein via a disulfide exchange reaction.

FRET Assay of Membrane-Binding Affinity. Membrane-binding constants for cysteine and spin-labeled C2 domains were determined using a fluorescence resonance energy transfer (FRET) experiment as previously described (*19*, *38*). Solutions containing C2 domain (0.5 μM) in standard assay buffer with saturating Ca^{2+} (1 mM) were titrated with a solution of phospholipid vesicles containing a 3:1 mole ratio of POPC/POPS and 5 mol % dansyl-PE suspended in standard assay buffer. The standard assay buffer contained 20 mM HEPES, 100 mM KCl, pH 7.4. For measurements characterizing unlabeled, cysteine-substituted C2 domains, the assay buffer also contained 5 mM DTT to reduce the spin-label from the protein. The intrinsic tryptophan donor in the C2 domain was excited at 284 nm, and the fluorescence of the dansyl-PE acceptor was monitored at 520 nm in a SLM-48000 spectrofluorimeter at 25 °C with excitation and emission slit widths at 4 and 8 nm, respectively. The direct excitation of the dansyl-PE was subtracted from the total fluorescence measured to yield the fluorescence due to protein-to-membrane FRET from docked C2 domains.

Plots of protein-to-membrane FRET as a function of total phospholipid concentration were subjected to nonlinear least-squares analysis in Kaleidagraph 3.5 (Synergy) using a homogeneous single-site binding curve to calculate the apparent dissociation constant (K_D) for phospholipids. Binding constants are normalized relative to the wild-type binding constant determined in parallel.

EPR Spectra and Calculation of Scaled Mobility Parameters. EPR spectra were acquired using a Bruker ESP300E X-band spectrometer (9.4 Ghz) equipped with a loop−gap resonator (Medical Advances). Samples were placed in quartz capillaries immediately before spectral acquisition at 23 °C. Samples contained 20−200 μM protein with either (1) 5 mM EDTA for apo protein samples, (2) 2 mM $CaCl_2$ for Ca^{2+}-loaded protein samples, or (3) 2 mM $CaCl_2$ and 40 mM phospholipids (3:1 PC/PS) for membrane-docked samples in standard assay buffer (see previously). Acquired EPR spectra are an average of four 4 min scans (2048 points), scanning over a range of 100 G, with an incident microwave power of 2.0 mW. For each spectrum, the peak-to-peak line width of the central EPR resonance (δ) was measured and used to calculate a scaled mobility factor using the relationship

$$M_s = \frac{(\delta^{-1} - \delta_i^{-1})}{(\delta_m^{-1} - \delta_i^{-1})} \quad (1)$$

where δ is the peak-to-peak line width of the central EPR resonance ($M_I = 0$), and δ_i and δ_m are calibration line widths of very immobile and very mobile labels, respectively (*39*). The calibration line widths used were standard values of $\delta_i = 8.4$ G and $\delta_m = 2.1$ G (*40*). The resulting scaled mobility factor operationally determines the apparent relative mobility of a given spin-label, inferred from its line width, using a standard mobility scale developed for MTSSL spin-labels coupled to proteins.

EPR Power Saturation Measurements of Membrane Penetration. For EPR continuous-wave power saturation experiments, samples were placed in TPX capillaries (Medical Advances) and equilibrated for 15 min with (a) nitrogen, (b) house air (20% O_2), or (c) nitrogen and 10 mM NiEDDA. Each EPR spectrum was obtained in a single 2 or 4 min 15 G scan (1024 points), taken at powers ranging from 0.2 to 80 mW with sample conditions as indicated for standard EPR spectra (ref *32*). For each spectrum, the peak-to-peak amplitude of the central resonance ($M_I = 0$) was recorded. The amplitudes of the EPR spectra were plotted as a function of microwave power and fit to the following equation as previously described (*32*, *41*):

$$A = \frac{C\sqrt{P}}{\left[1 + (2^{-\epsilon} + 1)\frac{P}{P_{1/2}}\right]^{\epsilon}} \quad (2)$$

where A is the peak-to-peak amplitude of the central EPR resonance, C is a scaling factor, P is the microwave power, $P_{1/2}$ is the power at which half-saturation occurs, and ϵ is a measure of the homogeneity of saturation. The best-fit $P_{1/2}$ values were then used to calculate a collision parameter for oxygen and NiEDDA as previously described (*32*, *41*)

$$\Pi(O_2) = \frac{P_{1/2}(O_2)/\Delta H_{pp}(O_2) - P_{1/2}(N_2)/\Delta H_{pp}(N_2)}{P_{1/2}(DPPH)/\Delta H_{pp}(DPPH)} \quad (3)$$

where $\Pi(O_2)$ is the collision parameter for oxygen, $P_{1/2}$ is the half-saturating power, and ΔH_{pp} is the peak-to-peak line width of the EPR signal at low microwave power. The collision parameter is normalized to a solid sample of DPPH (1,1-diphenyl-2-picrylhydrazyl) to correct for spectrometer differences. The collision parameters for oxygen and NiEDDA were used to calculate a depth parameter Φ for each spin-label as previously described (*32*, *41*)

$$\Phi = \ln\left(\frac{\Pi(O_2)}{\Pi(NiEDDA)}\right) \quad (4)$$

Reported depth parameters are a weighted average of duplicate experiments each using at least 20 different microwave powers. The weights used during averaging were inversely proportional to the square of the errors propagated from uncertainties in measurement of $P_{1/2}$ and ΔH_{pp} in the different environments (*42*).

Depth parameters for spin-labeled lipids were corrected for the leaflet effect by subtraction of a fixed quantity (ln 2), based on the following observations. In a system in which a highly polar zwitterion such as NiEDDA is added to membrane vesicles, diffusion across the membrane bilayer is very slow. As a result, the outer leaflet of the membranes is exposed to NiEDDA, while the inner leaflet is effectively shielded from NiEDDA. For membrane-binding C2 domains that are added to the preformed vesicles, the spin-labels on the domains interact only with the outer leaflet exposed to NiEDDA and thus experience a homogeneous environment. In contrast, for spin-labeled lipids incorporated into the vesicles, the spin-labeled lipids in the outer leaflet are exposed to NiEDDA, but the labeled lipids in the inner leaflet are inaccessible to NiEDDA and thus represent a separate population. Assuming that the two populations of spin-labeled lipids contribute equally to the measured EPR spectrum, which is a reasonable assumption since lipids are incorporated approximately equally into the inner and outer

leaflets of the membrane, the power saturation curve is the sum of the equally weighted curves for the two populations. Simulations of power saturation curves carried out in Kaleidagraph (not shown) indicate that when the difference in saturating power between the two populations is small, as is the case for labels in the hydrophobic membrane interior where the NiEDDA concentration is low even for the outer leaflet, the measured $P_{1/2}$ in the presence of NiEDDA is simply the average of the $P_{1/2}$ values of lipids exposed to and shielded from NiEDDA, respectively. It follows that the measured apparent NiEDDA collision parameter for spin-labeled lipids in vesicles is half the true collision parameter for the labeled lipids in the outer leaflet. To correct this artifact, the quantity ln 2 must be subtracted from the depth parameter for each spin-labeled lipid.

Determination of Membrane-Docking Geometry. To generate a membrane-docking model incorporating all 24 spin-labeled sites used in the analysis, the crystal structure of $cPLA_2$ (PDB 1rlw) was modified by changing each spin-labeled site to cysteine using the Biopolymers module of Insight2000 (Accelrys). The cysteines were each modified with the addition of an energy-minimized MTSSL moiety to generate a model of the spin-labeled site. The spin-labels were adjusted to the gauche+, gauche+ (g+, g+) conformation, which is the most prevalent conformation observed in crystallographic studies of the spin-labeled T4 lysozyme (*43*). By convention, in this conformation the side chain dihedral angles along the Cα−Cβ and Cβ−Sγ bonds are each +300° (*43*). For simplicity, the protein was translated to place an atom near the center of the domain, the β-carbon of residue 46, at the origin of the crystallographic coordinate system that defined the Cartesian axes of the laboratory frame. A starting position for the docking model was generated by placing the headgroup phosphate layer of an imaginary membrane perpendicular to the laboratory *y*-axis and passing through the origin, so that the protein starts partially imbedded in the membrane. A separate molecular coordinate system was defined with its *x*′-, *y*′-, and *z*′-axes identical to the laboratory *x*-, *y*-, and *z*-axes, respectively. Finally, the molecular *x*′-, *y*′-, and *z*′-coordinates of each nitroxide nitrogen in the molecular frame were tabulated for analysis. During subsequent domain rotations and translations in the laboratory frame, these molecular coordinates remained unchanged.

To determine the optimal protein geometry relative to the membrane surface, the depth parameters of different protein and lipid nitroxides were described by a single multivariate equation, which describes both the transformations of the protein model and the invariance of the lipid positions. The form of the equation was based on the known linear relationship between the depth parameter and the membrane depth (*41*). The equation possesses one dependent variable (Φ), five independent variables (*x*′, *y*′, *z*′, *P*, and *D*), and five unknowns (θ_x, θ_z, Y_{trans}, *m*, and *I*):

$$\Phi = m(x' \sin\theta_z + y' \cos\theta_z \cos\theta_x - z' \cos\theta_z \sin\theta_x + PY_{trans} + D) + I \quad (5)$$

Together, the terms in parentheses define membrane depth, or the distance of a given nitroxide from the headgroup phosphate layer after the protein is rotated clockwise through an angle θ_x about the laboratory *x*-axis, rotated clockwise through an angle θ_z about the laboratory *z*-axis, and translated along the laboratory *y*-axis by Y_{trans}, where the rotational directions are defined by an observer sitting at the molecular origin of the rotational axis and looking toward the positive end. The first three terms in parentheses represent the projection of the vector from the molecular origin to the nitroxide nitrogen onto the laboratory *y*-axis used to define the distance to the headgroup phosphate layer. The fourth term represents the translation of the entire protein toward the membrane and is nonzero only for protein nitroxides since *P* is set to unity for protein spin-labels and to zero for lipid spin-labels. The fifth term denotes the previously published distance *D* of a given lipid spin-label from the plane of the membrane phosphates (*44*) and is set to zero for protein nitroxides. Finally, the *m* and *I* parameters represent the slope and intercept of the linear relationship. Nonlinear least-squares fitting of the multivariate equation to determine the best-fit values of θ_x, θ_z, Y_{trans}, *m*, and *I* was performed using Igor Pro (Wavemetrics), yielding a self-consistent set of depth parameters linearly related to membrane depth, with the same slope and intercept for both protein and lipid spin-labels.

Comparison of Docking Tilt Angles and Depths. To compare the orientations of C2 domains derived from different PDB coordinate files, which define different C2 domain structures and starting orientations, three atoms in structurally analogous positions were chosen in one of the two β-sheets. Two of these atoms were located in the longest β-strand in the domain, which is strand 2 or 1 in type I or II C2 domains, respectively (*4*, *22*, *23*, *28*, *29*). The third atom is located in the furthest strand in the same sheet, which is strand 8 or 7 in type I or II C2 domains, respectively. The selected atoms were the α-carbons in residues 20, 27, and 118 in $cPLA_2$, residues 158, 165, and 256 in synaptotagmin I, and residues 173, 180, and 271 in protein kinase Cα. Two molecular vectors were then defined for each domain, a *z*′-vector extending from the first atom in strand 2(1) to the second atom in strand 2(1) and an *x*′-vector passing through the atom in strand 8(7) and perpendicular to the first vector. A molecular coordinate system was then defined, with its center at the first α-carbon, the *z*′-axis parallel to the *z*′-vector, and the x′-axis parallel to the *x*′-vector. Subsequently, each domain was oriented relative to an imaginary planar membrane surface in two different ways. First, the domain was placed in a common starting orientation with its *z*′-axis normal to the membrane and the center of the molecular coordinate system at a distance of 50 Å below the headgroup phosphate plane. This starting orientation places the domain outside the membrane with its calibration β-sheet perpendicular to the membrane surface and is the same for different domains. Second, the domain was placed at the appropriate membrane depth in its final docking orientation as defined by the previously published docking model for that domain (*32*, *35*, *45*). Last, the transformations needed to change the starting orientation into the final modeled orientation were calculated as a rotation about the *x*′-axis followed by a rotation about the *z*′-axis, then by a translation along the membrane normal. The resulting *x*′ and *z*′ rotational angles allow direct comparison of the angular differences between docking models. To compare the membrane penetration depths of different models, for each model the average depth of the multiple bound Ca^{2+} ions was determined, and the depth of the most deeply buried protein α-carbon was also

measured, where both depths were relative to the headgroup phosphate layer.

RESULTS

Mutagenesis, Spin-Labeling, and Purification of the C2 Domain of cPLA$_2$. Single cysteines were introduced into the C2 domain of human cPLA$_2$ at each position in the Ca^{2+}-binding loop I (residues 31−41 and 43), Ca^{2+}-binding loop II (residues 63−68), and Ca^{2+}-binding loop III (residues 93−101). In addition to six cysteine substitutions from a previous study, 21 new cysteine substitutions were generated to fully sample all 27 positions of the three Ca^{2+}-binding loops. Each cysteine mutant was overexpressed in *E. coli*, isolated as inclusion bodies**,** solubilized in a buffer containing urea and the spin-label MTSSL to simultaneously solubilize and label the protein, and dialyzed to refold the labeled protein. The active C2 domain was purified by affinity chromatography on a phosphatidylcholine (PC) lipid affinity column in the presence of saturating Ca^{2+}, which removes the improperly folded C2 domain and contaminating proteins (*19*, *32*).

Of the 27 mutant proteins possessing single cysteine residues in the three Ca^{2+}-binding loops, three failed to bind the lipid affinity column in both their reduced and spin-labeled forms (D40C, D43C, D93C). These three mutants each convert a Ca^{2+}-coordinating aspartate to a cysteine and presumably disrupt Ca^{2+}-dependent phospholipid binding by inhibiting Ca^{2+} binding. As a result, they were not utilized in the present study. The reduced and spin-labeled forms of the remaining 24 mutant proteins each bound in a Ca^{2+}-dependent fashion both to the lipid affinity column and to phospholipid vesicles, thereby ensuring they were active, folded proteins.

Membrane Affinities of Cysteine-Substituted and Spin-Labeled C2 Domains. For the mutant proteins that retained Ca^{2+}-triggered lipid binding, membrane-docking affinities were measured for both the free cysteine state and the spin-labeled state using a fluorescence resonance energy transfer (FRET) assay developed for membrane-docking proteins (*19*, *38*). Briefly, a Ca^{2+}-loaded C2 domain possessing a single intrinsic tryptophan used as an energy transfer donor was titrated with membrane vesicles composed of a 3:1 mole ratio of PC/PS, closely approximating the mole ratio of these lipids in eukaryotic membranes. The vesicles also contained 5 mol % dansylated PE, which served as an energy transfer acceptor. As the dansylated membranes were titrated into the sample, the increasing protein-to-membrane FRET yielded a homogeneous single-site binding curve, which was best-fit to determine the phospholipid binding constant (K_B).

Table 1 summarizes the resulting phospholipid binding constants of the 24 cysteine-substituted and 24 spin-labeled proteins, each relative to the wild-type binding constant. In 44 of the 48 cases, the relative binding constants reveal that the variant proteins possess membrane affinities within 3-fold of the wild-type, indicating that these perturbations are not significantly larger than the thermal energy ($\Delta\Delta G < 1.1RT$, where $RT = 0.6$ kcal/mol is the thermal energy at the experimental temperature). Such small perturbations are consistent with current models proposing that the protein−membrane interface involves a large surface of the protein and multiple side chains (*31*, *32*), so that modification of one side chain leaves most of the docking surface intact. In the remaining four cases, specifically two cysteine substitutions (F35C and Y96C) and two spin-label modifications (T31R1 and N64R1), modification causes a 3−6-fold loss of membrane affinity. Each of these four affinity losses correspond to modest perturbations only slightly larger than the thermal energy ($\Delta\Delta G$ from $1.1-1.9RT$). The affinity decreases observed for cysteine substitution at positions F35 and Y96 have been observed previously (*31*, *32*) and are consistent with the loss of bulky, hydrophobic Phe and Tyr residues on the membrane-binding face of the domain. At both these positions, coupling of the spin-label restores hydrophobicity and restores the affinity nearly to the wild-type level. The other two affinity losses observed for spin-label coupling at positions T31 and N64 are more difficult to rationalize and may arise from several factors such as the perturbation of a loop structure by a larger side chain or disruption of specific interactions with lipid headgroups. All four of the moderate affinity losses were due to a perturbed interaction between the Ca^{2+}-loaded protein and the membrane since separate experiments (not shown) indicated that the concentration of Ca^{2+} used in the titrations (1 mM) was sufficient to saturate the Ca^{2+}-binding site of the free domain in each of the four cases.

Focusing on the 24 spin-labeled proteins that were successfully isolated, even the largest perturbations of membrane affinity were comparatively small, and membrane binding could be driven to completion by the addition of sufficient membranes in each case. Thus, all 24 of the spin-labeled proteins were used in further EPR studies.

Table 1: Membrane Affinities of the Modified cPLA$_2$ C2 Domains

position	loop[a]	K_B(Cys)/K_B(WT)[b]	K_B(R1)/K_B(WT)[b]
WT		1	1
T31	I	0.5 ± 0.1	0.30 ± 0.05
K32	I	0.8 ± 0.3	0.8 ± 0.3
G33	I	0.45 ± 0.07	0.37 ± 0.07
A34	I	1.6 ± 0.6	1.4 ± 0.5
F35	I	0.19 ± 0.02	0.6 ± 0.1
G36	I	3 ± 1	1.4 ± 0.3
D37	I	1.2 ± 0.2	1.3 ± 0.2
M38	I	0.6 ± 0.1	0.7 ± 0.1
L39	I	0.57 ± 0.07	1.4 ± 0.2
T41	I	0.6 ± 0.1	0.4 ± 0.1
F63	II	0.4 ± 0.1	0.5 ± 0.1
N64	II	0.9 ± 0.2	0.16 ± 0.03
N65	II*	0.45 ± 0.04	0.36 ± 0.04
D66	II	0.8 ± 0.2	0.9 ± 0.3
I67	II	1.0 ± 0.3	0.8 ± 0.2
N68	II	1.2 ± 0.3	0.7 ± 0.1
A94	III	0.4 ± 0.1	0.4 ± 0.1
N95	III*	0.34 ± 0.04	0.9 ± 0.2
Y96	III	0.18 ± 0.03	0.8 ± 0.1
V97	III	0.5 ± 0.1	0.9 ± 0.3
M98	III	0.7 ± 0.2	0.9 ± 0.3
D99	III	0.6 ± 0.1	0.6 ± 0.1
E100	III	0.6 ± 0.1	0.47 ± 0.06
T101	III	1.2 ± 0.3	0.6 ± 0.1

[a] Location indicates the Ca^{2+}-binding loop containing the cysteine substitution. Positions at which the native side chain coordinates Ca^{2+} are indicated by an asterisk (*). [b] Membrane affinities are shown as the binding affinity of the cysteine mutant or the spin-labeled cysteine mutant relative to wild-type membrane binding affinity, as determined by FRET (see Materials and Methods). The average wild-type membrane binding constant was $K_B = (6 \pm 1) \times 10^4\ M^{-1}$, corresponding to a dissociation constant of $K_D = 17 \pm 4\ \mu M$. Experiments were performed with 0.5 μM protein in 20 mM HEPES, 100 mM KCl, 1 mM $CaCl_2$, pH 7.4, 25 °C. Buffers also contained 5 mM DTT for unlabeled cysteine mutants.

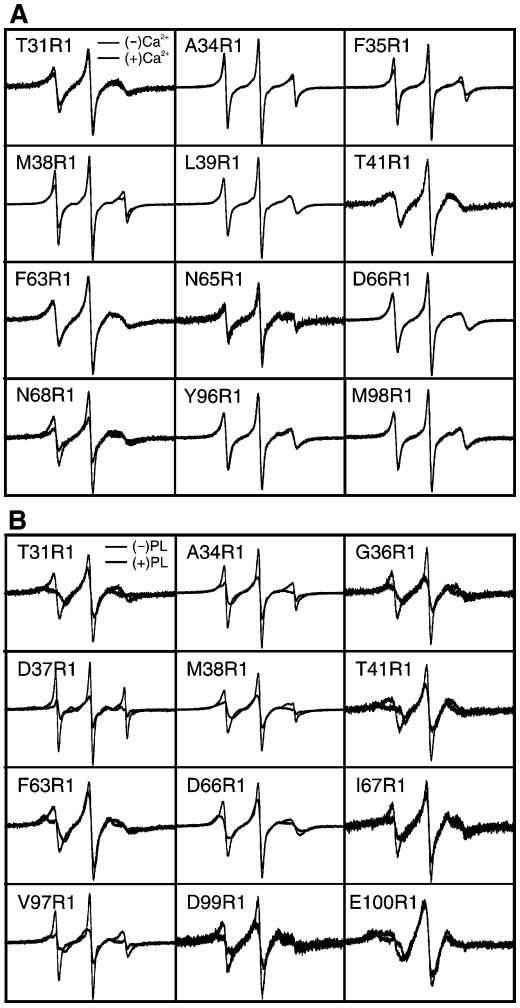

FIGURE 2: Effects of Ca^{2+} binding and membrane docking on EPR spectra. (A) Shown are EPR X-band spectra for spin-labeled C2 domains acquired in the presence of 5 mM EDTA (thin line) or 2 mM $CaCl_2$ (heavy line) for 12 representative modified proteins. (B) Shown are EPR spectra for spin-labeled C2 domains acquired in the presence of 2 mM $CaCl_2$ without (thin line) or with (heavy line) 40 mM PC/PS membranes for 12 representative modified proteins. Samples contained 20−200 μM protein in 20 mM HEPES, 100 mM KCl, pH 7.4, and spectra were acquired at 23 °C.

Effects of Ca^{2+} Binding on EPR Spectra. EPR spectra were obtained for each spin-labeled domain in the presence or absence of saturating Ca^{2+}, revealing the effects of Ca^{2+} on nitroxide probes at 24 Ca^{2+}-binding loop positions. In most cases, the spectral differences between the apo and the Ca^{2+}-loaded protein are undetectable, but small Ca^{2+} effects are observed at specific positions. Figure 2A overlays apo and Ca^{2+}-loaded spectra for 12 representative domains (compare with the much larger changes triggered by membrane docking in Figure 2B). The largest of the Ca^{2+}-triggered effects are observed at three positions in the first and second Ca^{2+}-binding loops. These Ca^{2+} effects are too small to quantitate using scaled mobility factors (Figure 3) but are detectable in spectral overlays as illustrated in Figure 2A. In particular, two positions in the first Ca^{2+}-binding loop exhibit spectral broadening in the presence of Ca^{2+} (F35R1 and M38R1). These positions both localize to the solvent-exposed face of the loop I helix observed in structures of the Ca^{2+}-occupied domain. Such findings suggest that the helix is present in the apo as well as the Ca^{2+}-occupied domain since spectral

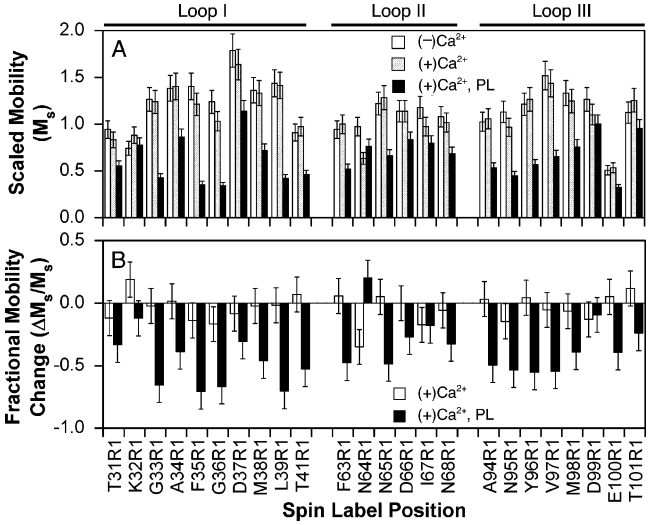

FIGURE 3: Scaled mobilities of C2 domain spin-labels. The scaled mobility of a specific spin-label position was determined from the peak-to-peak line width of its central transition (δ). This line width was compared to standard line widths for highly mobile and immobile spin-labels to calculate the scaled mobility (M_s) using the relationship $M_s = (\delta^{-1} - \delta_i^{-1})/(\delta_m^{-1} - \delta_i^{-1})$, where $\delta_i = 8.4$ G and $\delta_m = 2.1$ G are the standard calibration line widths (*39*). (A) Scaled mobility parameters for EPR spectra of labeled C2 domains without Ca^{2+} (open), with Ca^{2+} (hatched), and with both Ca^{2+} and phospholipid membranes (closed). (B) Fractional change in scaled mobility, calculated as $[(M_s(Ca^{2+}) - M_s(apo))/M_s(apo)]$ (open) or as $[(M_s(PL) - M_s(Ca^{2+}))/M_s(Ca^{2+})]$ (closed). EPR parameters and sample conditions are as in Figure 2.

changes would likely be observed throughout the helical region if helix formation were induced by Ca^{2+} binding. The simplest explanation is that Ca^{2+} binding slows the internal breathing motions of a preexisting helix. This subtle slowing would decrease the mobilities of the perturbed residues on the solvent-exposed helix face, yielding the observed spectral broadening. Smaller effects would be expected for positions on the opposite helix face, where contacts with the protein would constrain side chain mobilities in both the apo and the Ca^{2+}-occupied states. The third perturbed position lies at the end of loop II (N68R1) and becomes sharper on the addition of Ca^{2+}, suggesting that the side chain or backbone at this position becomes more mobile in the Ca^{2+}-bound state. Such a loop terminus could act as a hinge for Ca^{2+}-triggered loop movements with respect to the main body of the protein. Overall, however, since Ca^{2+} binding has little or no effect at 21 of the 24 positions tested, the EPR evidence suggests that the Ca^{2+} binding triggers only small, localized changes in loop dynamics or small, rigid body movements of the loops via hinge flexibility.

Effects of Membrane Docking on EPR Spectra. EPR spectra were also acquired in the presence and absence of phospholipid membranes (PC/PS mole ratio 3:1) under saturating Ca^{2+} conditions. Representative spectra are shown in Figure 2B for 12 of the 24 spin-labeled domains. Membrane docking causes large increases in the spectral line widths at nearly all labeling sites, indicating a general loss of spin-labeled mobility. The relative mobilities of spin-labels are compared in Figure 3 using the scaled mobility factor, which compares the width of the central resonance to standard values for immobilized and rapidly tumbling spin-labels (*39*, *40*). Scaled mobility factors over 1.0 are observed at many positions in the apo and Ca^{2+}-loaded domain,

indicating that the tumbling of the free domain contributes to the observed mobility. For 23 of the 24 spin-labeled domains, membrane docking reduces the scaled mobility factor between 10 and 70%, consistent with a decrease in the global tumbling of the domain upon docking to a large phospholipid vesicle. The largest docking-induced mobility losses are observed for positions in the helical region of the first Ca^{2+}-binding loop, followed by positions in the third Ca^{2+}-binding loop, while positions in the second Ca^{2+}-binding loop show the smallest mobility losses. These findings are consistent with the insertion of the most perturbed spin-labels into a more viscous and hydrophobic environment such as the phospholipid membrane, which would slow the local tumbling of the spin-label as well as the global tumbling of the domain.

EPR Depth Parameters and Relative Depths of Membrane Insertion. Depth parameters for the spin-labeled C2 domains were measured by continuous-wave EPR power saturation measurements for membrane-docked C2 domains (i) in the presence of molecular O_2, (ii) in the presence of NiEDDA, and (iii) in the absence of both paramagnetic relaxing agents (*32*, *41*). This approach makes use of the fact that collisions with a soluble paramagnetic probe increases the spin−lattice relaxation rate of the spin-label, which can be detected as an increase in the microwave power needed to saturate the EPR signal. Since O_2 preferentially partitions into the hydrocarbon phase of the bilayer, spin-labels inserted into the membrane exhibit higher saturation powers when O_2 is added. Similarly, spin-labels exposed to water exhibit higher saturation powers when NiEDDA is added. The half-saturating power for each measurement, together with the line width of the EPR spectrum, was used to calculate a collision parameter Π proportional to the collision rate for each paramagnetic reagent [$\Pi(O_2)$ and Π(NiEDDA), respectively]. Subsequently, the ratio of the collision parameters was used to calculate the depth parameter Φ at each spin-labeled position ($\Phi = \ln[\Pi(O_2)/\Pi(\text{NiEDDA})]$). The depth parameter is positive for spin-labels deeply buried in the membrane where collision rates with O_2 are high and negative for spin-labels in the aqueous phase where collision rates with NiEDDA are high.

The collision and depth parameters for each spin-labeled cysteine are summarized in Table 2 and Figure 4. The depth parameters vary from +2.4 to −1.8, indicating that the spin-labels are exposed to a wide range of environments extending from locations inside the membrane to locations fully exposed to water. The observed differences between depth parameters are defined primarily by the NiEDDA collision parameter, which exhibits a 6-fold larger range than the O_2 collision parameter as observed previously (*32*).

Figure 4 shows the EPR depth parameters plotted as a function of spin-label position for each of the three Ca^{2+}-binding loops. The spin-labels located in Ca^{2+}-binding loop I exhibit the most variation in depth parameters. At either end of the loop, the EPR depth parameters are negative, indicating that these positions are more exposed to an aqueous environment. The spin-labels in the middle of the loop have depth parameters that are considerably more positive, reaching values as high as $\Phi = +2.4$. These positive values are the largest encountered among the tested positions, indicating that loop I inserts most deeply into the membrane hydrocarbon. Moreover, the interior of the loop exhibits an oscillating pattern of depth parameters that is characteristic of helical structure. This indicates that the short α-helix observed in the crystal and NMR structures of the domain remains intact in the membrane-bound protein.

Depth parameters for labels in loop II are all negative and indicate that this loop is significantly exposed to solvent in the membrane-docked state. Here, the largest value of the depth parameter is $\Phi = -0.8$, which is consistent with a location in the headgroup layer but not the hydrocarbon layer. While there is variability between the depth parameters of different positions, the values are in a range where the depth parameter varies little with distance from the membrane surface (*32*). Therefore, while it is clear that Ca^{2+}-binding loop II interacts with the headgroup layer, the negative depth parameters measured for this loop are less useful than the positive values measured for loops I and III for determining the depth and orientation of the domain relative to the membrane surface.

Table 2: Collision and Depth Parameters for Spin-Labeled cPLA$_2$ C2 Domains[a]

position	Ca^{2+} binding loop	$\Pi(O_2)$	Π(NiEDDA)	depth parameter $\Phi = \ln[\Pi(O_2)/\Pi(\text{NiEDDA})]$[b]
T31	I	0.19 ± 0.05	0.9 ± 0.1	−1.5 ± 0.2
K32	I	0.27 ± 0.05	0.28 ± 0.06	−0.1 ± 0.1
G33	I	0.19 ± 0.03	0.61 ± 0.05	−1.00 ± 0.07
A34	I	0.36 ± 0.06	0.24 ± 0.05	0.4 ± 0.1
F35	I	0.51 ± 0.06	0.08 ± 0.03	1.9 ± 0.2
G36	I	0.32 ± 0.05	0.08 ± 0.03	1.5 ± 0.2
D37	I	0.29 ± 0.05	0.33 ± 0.05	−0.3 ± 0.1
M38	I	0.47 ± 0.05	0.18 ± 0.02	0.94 ± 0.07
L39	I	0.55 ± 0.05	0.05 ± 0.02	2.4 ± 0.2
T41	I	0.22 ± 0.03	1.0 ± 0.1	−1.5 ± 0.1
F63	II	0.28 ± 0.05	1.1 ± 0.1	−1.4 ± 0.1
N64	II	0.25 ± 0.04	0.9 ± 0.1	−1.2 ± 0.1
N65	II	0.25 ± 0.08	0.5 ± 0.1	−0.8 ± 0.2
D66	II	0.27 ± 0.04	1.4 ± 0.1	−1.6 ± 0.1
I67	II	0.21 ± 0.06	0.9 ± 0.1	−1.4 ± 0.2
N68	II	0.22 ± 0.05	1.3 ± 0.1	−1.8 ± 0.1
A94	III	0.15 ± 0.07	0.3 ± 0.1	−0.5 ± 0.2
N95	III	0.19 ± 0.04	0.16 ± 0.03	0.2 ± 0.1
Y96	III	0.35 ± 0.06	0.11 ± 0.04	0.8 ± 0.2
V97	III	0.42 ± 0.07	0.15 ± 0.04	1.0 ± 0.2
M98	III	0.27 ± 0.04	0.20 ± 0.05	0.3 ± 0.1
D99	III	0.14 ± 0.07	0.21 ± 0.07	−0.5 ± 0.3
E100	III	0.13 ± 0.06	0.48 ± 0.07	−1.1 ± 0.2
T101	III	0.17 ± 0.04	0.9 ± 0.1	−1.7 ± 0.2

[a] Collision parameters (Π) were measured using EPR continuous-wave power saturation as described in the Materials and Methods. EPR samples contained 20−150 μM (typically 50 μM) C2 domain in 20 mM HEPES, 100 mM KCl, 2 mM $CaCl_2$, 40 mM phospholipid (3:1 ratio PC/PS), pH 7.4, 25° C. Indicated Π values correspond to an error-weighted average of individual values determined from duplicate experiments. Errors of the individual values were calculated using a standard method of error propagation from the individual errors in $P_{1/2}(O_2)$ and $P_{1/2}$(NiEDDA) determined by the best-fit of the measured power saturation curve (see Materials and Methods). Finally, the indicated errors were calculated using a standard method of error calculation for the weighted average of two data points with known individual errors (*42*). [b] Indicated depth parameters (Φ) are an error-weighted average of individual values determined from duplicate experiments. Errors of the individual values were calculated using a standard method of error propogation from the individual errors in $\Pi(O_2)$ and Π(NiEDDA) determined by the best-fit of the measured power saturation curve. Finally, the indicated errors were calculated from the two individual errors using a standard method of error calculation for the weighted average of two data points (*42*).

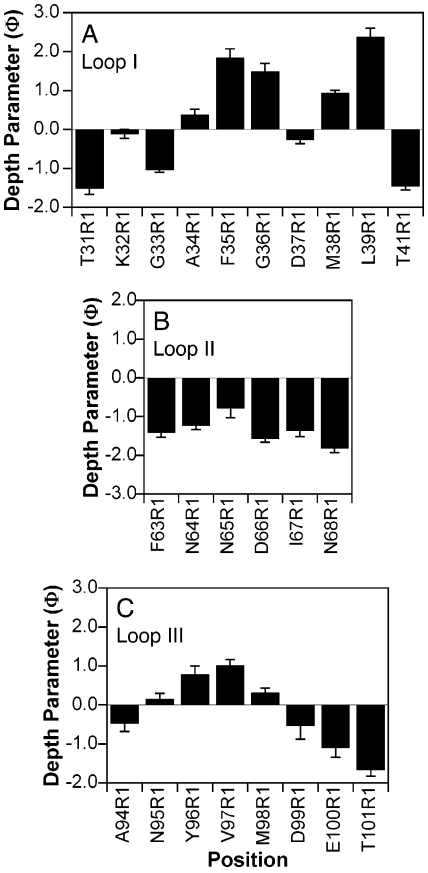

FIGURE 4: Continuous-wave power saturation depth parameters for the three Ca^{2+}-binding loops. (A) Ca^{2+}-binding loop I, (B) Ca^{2+}-binding loop II, and (C) Ca^{2+}-binding loop III. The depth parameter Φ is calculated as the log ratio of spin-label collision rates with dioxygen and with NiEDDA ($\Phi = \ln[\Pi(O_2)/\Pi(\text{NiEDDA})]$). EPR spectra were single 2 min scans, with sample conditions as in Figure 2. Measured values reflect the error-weighted average of duplicate experiments**,** using errors propagated from measurements of $P_{1/2}$ and ΔH_{pp} (see Materials and Methods). Errors in the average values shown were calculated as the inverse square root of the sum of the inverse squares of errors in individual measurements [error of mean $= (\sum(\text{individual error})^{-2})^{-1/2}$] (*42*).

The parameters for spin-labels at the ends of the Ca^{2+}-binding loop III are negative, but toward the middle of the loop they become increasingly positive, with a maximum value of $\Phi = +1.0$ for the spin-label at position V97, indicating that the loop inserts into the hydrocarbon layer, although less deeply than loop I. This corresponds well with a model in which the hydrophobic amino acids at the tip of the loop insert into the hydrocarbon phase, while the more hydrophilic amino acids at the ends of the loop interact with the headgroup region of the membrane or with water. This pattern of EPR depth parameters is also consistent with the simple hairpin-like conformation of the loop as it appears in the crystal structure of the domain.

Overall, these findings indicate that the depth parameters measured for spin-labels in the Ca^{2+}-binding loops of the C2 domain of $cPLA_2$ are consistent with the known crystal and solution structures of the domain in the absence of membranes (*22*, *23*). Thus, it is reasonable to use the structure of the free domain to model the depth and orientation of the membrane-bound domain. To calibrate this modeling, depth parameters were also measured for a set of four isomeric lipids, each containing the same nitroxide ring attached to a different acyl chain position (5-doxyl PC, 7-doxyl PC, 10-doxyl PC, and 12-doxyl PC). The burial depth in the membrane is accurately known for each of these lipid-attached nitroxides (*46*), providing a set of four distances with which to calibrate the protein depth parameters.

Modeling the Membrane-Docking Orientation and Penetration Depth of the C2 Domain. To model the membrane-docked domain, the crystal structure of the C2 domain of $cPLA_2$ (PDB 1rlw) (*22*) was first modified by replacing each residue for which a depth parameter was measured with cysteine, using the Biopolymer module of Insight 2001 (Accelrys). An energy-minimized MTSSL structure was attached to each cysteine, and the resulting side chain was adjusted to adopt the conformation most commonly observed for spin-labels in the crystal structure of the T4 lysozyme (*43*), corresponding to gauche dihedral angles of +300° about the first and second dihedral angles of the side chain (g+g+). The coordinates for the nitroxide nitrogen of each spin-labeled side chain were tabulated for use in subsequent calculations.

The following approach was developed to determine the rotations and translation needed to insert the crystal structure, together with its modeled spin-labeled side chains, into the membrane to produce a model of the protein-membrane docking geometry. The starting position was defined by first translating the domain until an atom near the center of the domain (the β-carbon of residue 46) lay at the origin of the crystallographic coordinate system, which was used to define the fixed Cartesian axes of the laboratory frame. Next, the headgroup phosphate layer of an imaginary planar membrane was placed perpendicular to the *y*-axis at the origin so that the domain was partially imbedded in the membrane. Subsequently, using the experimental depth parameters as a guide, the domain was rotated about the laboratory *x*-axis by angle θ_x, rotated about the laboratory *z*-axis by angle θ_z, and translated normal to the membrane along the laboratory *y*-axis by a distance Y_{trans} to place the nitroxide nitrogens at the optimum distances relative to the phosphate plane. This optimization process utilized the established linear relationship between depth parameter (Φ) and membrane penetration depth in the region where the depth parameter is positive (*41*). To focus solely on this linear region, protein positions possessing negative depth parameters were excluded from the optimization. The optimization focused solely on 14 spin-labels, a subset that included all the positions with positive depth parameters: loop I residues 34−39, loop III residues 95−98, and the four spin-labeled lipids. The optimization procedure independently varied the two protein rotational angles (θ_x, θ_z) and the translation distance normal to the membrane (Y_{trans}) to maximize the linearity of the depth parameter versus membrane-depth relationship for the protein data, as well as the collinearity of the protein data with the fixed lipid data points.

Figure 5A shows the plot of depth parameter (Φ) versus membrane penetration depth for the initial optimized docking model wherein the protein labels are all oriented in the g+g+ side chain conformation. This initial optimization yielded a reasonably linear relationship with a correlation coefficient of $R = 0.95$, but significant improvement was obtained by adjusting the side chain conformations of the spin-labels at just two positions, 97 and 98, from dihedral angles of +300°, +300° (g+g+) to −300°, +300° (g−g+), or +180°, +300°

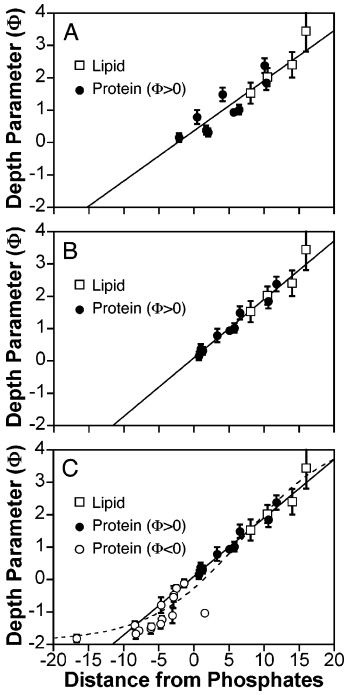

FIGURE 5: Depth parameter vs distance plots for spin-labeled lipids and C2 domains. Depth parameters for spin-labeled lipids (open squares) and spin-labeled proteins with positive depth parameters (closed circles) are plotted as a function of distance from membrane phosphates. (A) Depth parameter−distance plot for the model calculated with all spin-labels in a g+g+ conformation, focusing on spin-labels with positive depth parameters. Shown is the best-fit straight line for these data points. (B) Depth parameter−distance plot for the model calculated with the conformations of labels at V97R1 and M98R1 adjusted to g−g+ and tg+ conformations, respectively, while maintaining all other labels in a g+g+ conformation. Shown is the best-fit straight line for these data points, again focusing on spin-labels with positive depth parameters. (C) Plot including points for protein labels with negative depth parameters (open circles). Shown is the best-fit straight line from panel B that accurately describes spin-labels possessing positive depth parameters, located in a region ranging from the hydrocarbon phase to the deeper half of the headgroup layer (*41*, *57*). Also shown is the best-fit hyperbolic tangent function that provides a better model for the negative depth parameters observed in a region ranging from the aqueous half of the headgroup layer to the bulk aqueous phase (*32*).

(tg+), respectively. These two positions were targeted for adjustment since the membrane depths of their nitroxides in the initial model were significantly deeper than indicated by their measured depth parameters. Further optimization of the protein transformations θ_x, θ_z, and Y_{trans} yielded an improved docking model with a highly linear depth parameter versus membrane penetration depth relationship as shown in Figure 5B. In this improved model, the C2 domain crystal structure (again, PDB 1rlw) is rotated by $\theta_x = 33° \pm 6$ about the laboratory *x*-axis, $\theta_z = -124° \pm 3$ about the laboratory *z*-axis, and translated $Y_{trans} = 12 \pm 1$ Å out of the membrane relative to the starting position. The correlation coefficient for Figure 5B is $R = 0.99$, indicating that the described approach has successfully generated a self-consistent model for the membrane-docked C2 domain.

While the model of Figure 5B yields an excellent correlation between depth parameter and depth of insertion for protein spin-labels with positive depth parameters, this model yields poor correlation (not shown) for the protein labels with negative depth parameters that were omitted from the optimization procedure. Part of this deviation arises from the fact that in the negative region the depth parameter asymptotically approaches the value observed for the spin-label in bulk water so that a linear correlation is not expected in this region where the depth parameter becomes insensitive to distance and is better represented by a hyperbolic tangent function (*32*). Moreover, crystallographic evidence supporting the g+g+ spin-label conformation has been obtained only for spin-labels attached to α-helices, but none of the spin-label positions exhibiting negative depth parameters lie on the surface of an α-helix; thus, the conformations of these spin-labels could deviate significantly from the assumed starting conformation. The largest deviation from the correlation is at position 33, where the modeled nitroxide position is approximately 10 Å deeper in the membrane than its depth parameter would indicate. Notably, the crystal structure of the C2 domain (*22*) indicates that the native glycine at this position adopts a conformation with backbone dihedral angles ($\phi = 109°$, $\psi = 167°$) permitted only for glycine residues (*47*). Thus, replacement of Gly 33 with Cys likely perturbs the structure of CBL 1, yielding a depth parameter inconsistent with those measured for the surrounding spin-labels that are less perturbing. For the other 13 positions exhibiting negative depth parameters, a close fit to the hyperbolic tangent shape expected for this region was obtained by adjusting the conformations of eight spin-labels as needed (*32*), as illustrated in Figure 5C. This figure demonstrates that the backbone conformation of the crystal structure, together with the flexibility of the spin-label side chains, is able to adequately fit the experimental depth parameters, providing strong evidence against large rearrangements of the Ca^{2+}-binding loops upon membrane docking. These findings do not, however, rule out subtle movements of the loops (*48*, *49*) due to uncertainties in spin-label conformations.

The crystal structure of the C2 domain, with spin-labels colored according to depth parameter and modeled according to conformations used in the final docking model (Figure 5C), is shown in Figure 6. The model illustrates the transition from deeply membrane-embedded spin-labels in loops I and III, shown in red, to labels exposed to the aqueous phase, shown in dark blue. Overall, the visual correlation between depth parameter and position in the protein is very high, further supporting the conclusion that the crystal structure closely approximates the conformation of the membrane-docked protein.

DISCUSSION

Implications for the Structure of the apo C2 Domain. Although extensive structural information is available for the Ca^{2+}-occupied C2 domain of cPLA$_2$, the structure of the apo and membrane-docked states has not yet been elucidated. As a result, the structural changes triggered by Ca^{2+} and membrane binding are not yet known. The present study sheds light on the effects of Ca^{2+} binding on the side chain motions of 24 residues in the Ca^{2+}-binding loops. At 21 of the 24 loop positions, Ca^{2+} binding triggers little or no change in the EPR spectrum, strongly suggesting that that the domain retains a similar structure in the presence and absence of Ca^2. The three sites at which moderate changes occur are clustered into specific locations on the Ca^{2+}-binding loops, supporting the hypothesis that Ca^{2+} triggers small,

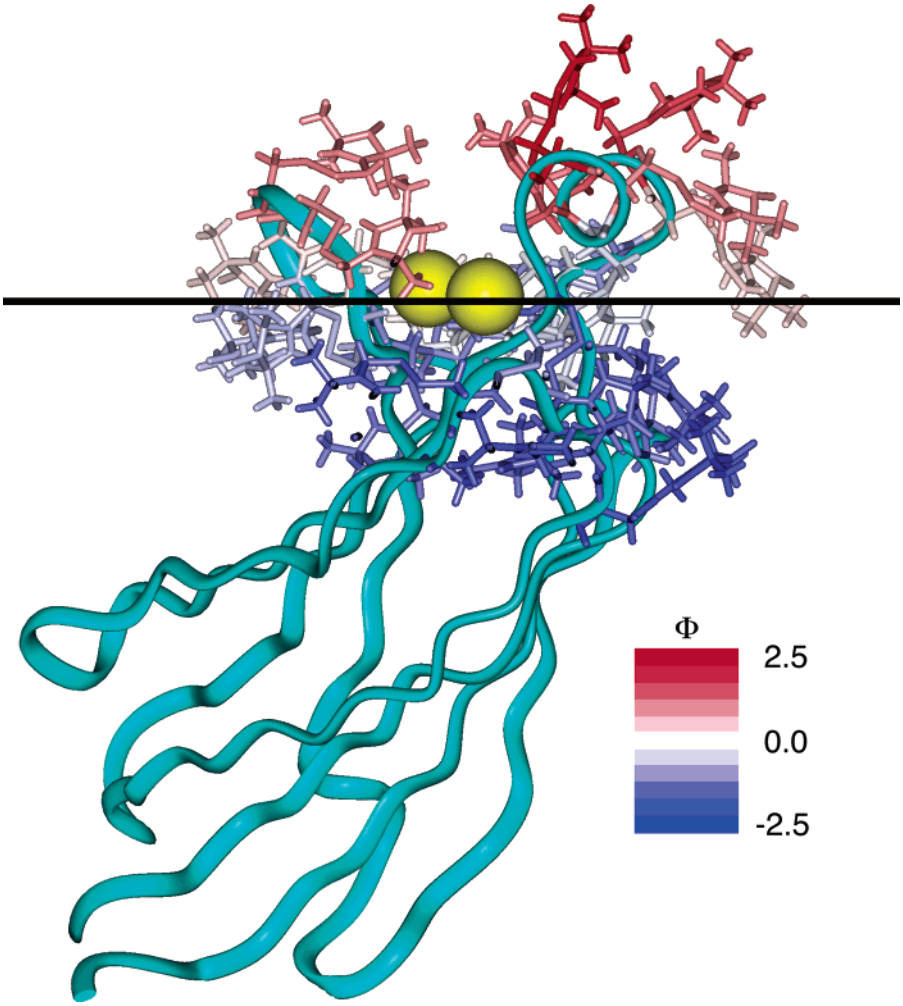

FIGURE 6: Orientation and depth of the C2 domain of $cPLA_2$ with respect to a membrane surface. The crystal structure of the C2 domain of $cPLA_2$ (*22*) is represented in cyan ribbons, with two Ca^{2+} ions shown as yellow spheres. The phosphate plane of the membrane is depicted as a solid line, such that the glycerol backbone and hydrocarbon core regions of the membrane lie above the line. Protein spin-labels oriented in their final optimized conformations are colored according to their measured depth parameters, with positive depth parameters indicated by increasing red and negative depth parameters indicated by increasing blue. The figure was generated using Insight2000 (Accelrys).

localized conformational changes. Overall, the EPR results strongly disfavor major Ca^{2+}-triggered movements or rearrangements of the Ca^{2+}-binding loops but cannot rule out minor changes in the position or dynamics of the loops relative to the main body of the protein.

Implications for the Structure of the Membrane-Docked C2 Domain. The EPR depth parameters measured for the membrane-bound C2 domain are remarkably consistent with the structure of the Ca^{2+}-occupied domain in the absence of membranes. Specifically, in the final optimized docking model there is a strong correlation of depth parameter with spin-label position in the crystal structure of the isolated Ca^{2+}-occupied domain (Figure 6). This correlation is observed for residues within each of the three Ca^{2+}-binding loops providing strong evidence that (1) the average conformations of the loops do not undergo large changes upon membrane docking and (2) the crystal structure of the isolated domain provides a suitable conformation for modeling the docking of the domain to the membrane surface. The data cannot rule out minor rigid movements of the loops relative to the main body of the protein upon membrane docking, but such changes are not necessary to generate an excellent fit of the isolated domain structure to the measured EPR depth parameters. Further experiments utilizing double spin-labeled mutants of the C2 domain will elucidate loop movements, if present.

The superposition of the C2 domain, with modeled spin-labels, onto a simulated phosphatidylcholine bilayer is shown in Figure 7. The calculated C2 domain orientation and insertion places the two Ca^{2+} ions within 1.0 Å of the plane of the membrane phosphates. This placement would optimize the electrostatic interaction between the Ca^{2+} ions and the headgroup phosphates, consistent with the idea that the phosphates provide direct Ca^{2+} coordination, thereby replacing some of the water molecules that coordinate Ca^{2+} ions bound to the free domain as proposed for other C2 domains (*29*, *30*). The modeled orientation and insertion indicates that most of the loop I helix and the tip of loop III insert into the hydrocarbon layer of the membrane, while other residues insert into the headgroup layer or are exposed to the aqueous phase. The modeled insertion must significantly perturb the positions and conformations of adjacent phospholipids, and the resulting displacement of phospholipids is consistent with observed increases in membrane surface pressure upon docking of the $cPLA_2$ C2 domain (*50*). Furthermore, it is likely that one or more phospholipid molecules occupy the

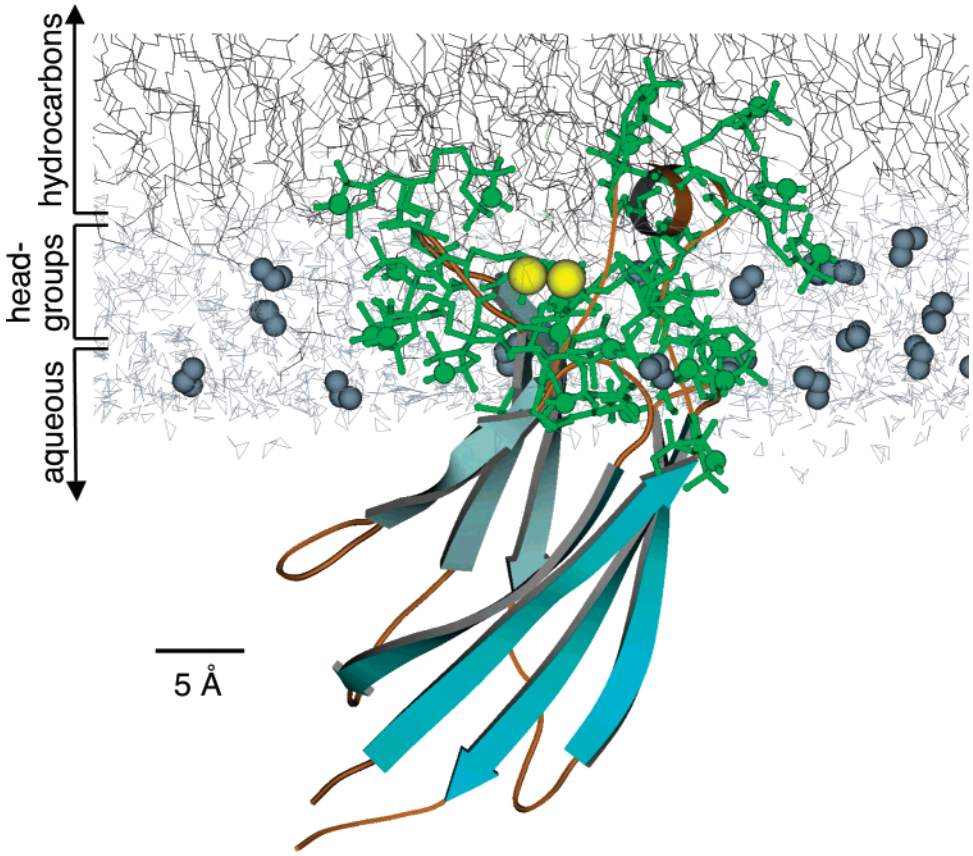

FIGURE 7: Modeled depth and orientation of the cPLA$_2$ C2 domain on a simulated membrane bilayer. The crystal structure of the C2 domain of cPLA$_2$ (*22*) with the final modeled spin-label conformations is superimposed on a simulated membrane bilayer (*59*, *60*). The β-strands of the protein are shown in cyan, with two Ca^{2+} ions in yellow spheres and protein spin-labels in green. The membrane is depicted with hydrocarbon chains in black and headgroup atoms and water molecules shown in gray. This schematic representation was generated in Molscript (*56*) using a modified protein crystal structure generated in Insight2000 (Accelrys).

cleft between the first and the third Ca^{2+}-binding loops in the docked state. However, the effects of C2 domain docking on local lipid structure have yet to be determined.

The proposed model for the membrane-docked C2 domain indicates that most of the helix in loop I and the tip of loop III interact with the hydrocarbon phase of the bilayer, while the other Ca^{2+}-binding loop residues interact with the headgroup region or the aqueous phase. This model is entirely consistent with the amino acid composition of the three loops. For instance, the helix in loop I contains three large hydrophobic residues (Phe 35, Met 38, Leu 39) and three smaller neutral residues (Gly 33, Ala34, Gly 36) that are proposed to insert into the membrane hydrocarbon. The remaining residues in loop I, which are proposed to interact with the headgroup region of the membrane (Thr 31, Lys 32, Asp 37, Asp 40, Thr 41), are all hydrophilic in nature. In the same manner, the three most deeply inserted residues in loop III (Tyr 96, Val 97, Met 98) are all large hydrophobic residues, while the remaining loop III positions (Asp 93, Ala 94, Asn 95, Asp 99, Glu 100, Thr 101) have a hydrophilic character consistent with the interaction with the headgroup region or with water. Interestingly, loop II also contains two large hydrophobic amino acids (Phe 63, Ile 67), but the EPR depth parameters indicate that these loop positions are too distant from the headgroup phosphate layer to penetrate into the hydrocarbon core. Instead, residue 63 is partially buried in the interior of the domain, while residue 67 may be involved in hydrophobic interactions with lipid headgroups as has been observed with apolar residues in the C2A domain of synaptotagmin I (*51*)**.** The remaining loop II residues (Asn 64, Asn 65, Asp 66, Asn 68) are hydrophilic, consistent with their modeled locations in the polar headgroup and aqueous regions.

Different Models of Orientation and Insertion of the C2 Domain of cPLA$_2$. A previous spin-labeling study utilized 13 sites scattered throughout the C2 domain of cPLA$_2$ to generate an initial orientation and depth of penetration for the membrane-docked C2 domain. In the present study, 24 positions in the three Ca^{2+}-binding loops were used to refine the docking model. The refinement yields significant improvements in both the depth of insertion and the angle relative to the membrane surface. The initial study placed the two Ca^{2+} ions approximately 3 Å beyond the plane of the membrane phosphates toward the hydrocarbon layer, while the Ca^{2+} ions in the present model lie in the headgroup layer within 1 Å of the phosphate plane. The previous study also placed Ca^{2+}-binding loops I and III at approximately equal depths in the membrane, whereas the present refinement reveals that Ca^{2+}-binding loop I penetrates significantly more deeply. Specifically, in the refined model the most deeply buried label on loop I (position 39) penetrates approximately 7 Å more deeply than the deepest label on loop III (position 97). This difference in loop depths gives rise to a notable difference in the β-strand tilt angle between the two models (see below).

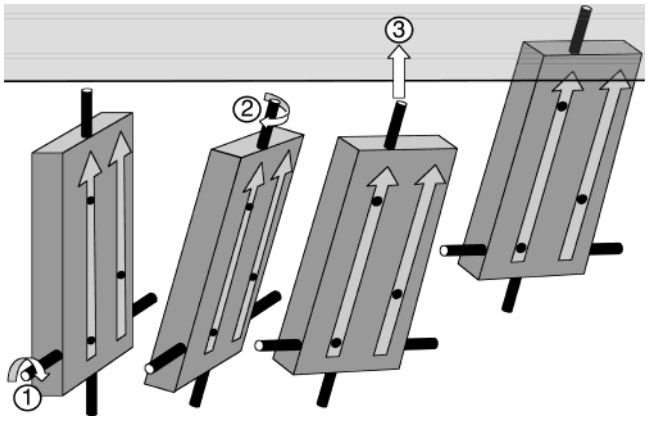

FIGURE 8: Rotations and translation used to compare different docking models. A C2 domain is depicted as a solid rectangle, with the three α-carbons used to define the molecular axes shown as circles and the molecular x'- and z'-axes shown as rods (see text). The membrane bilayer is shown in yellow. The universal starting position places the z'-axis normal to the membrane surface, such that the calibration β-sheet is perpendicular to the membrane, and fixes a calibration atom at a standard distance from the membrane. To transform this starting position into the final modeled position, the domain is rotated about the x'-axis, then rotated about the z'-axis to produce the final angular orientation, and subsequently is translated along the membrane normal to generate the final membrane penetration depth. Rotations and translations needed to reproduce the published docking models for the $cPLA_2$, PKCα, and SytIa C2 domains are compared in Table 3.

Table 3: Modeled Geometries of Membrane-Docked C2 Domains[a]

structure used for docking model	θ (deg)	φ (deg)	Z_{trans} (Å)	depth (Ca^{2+}) (Å)	deepest residue	depth (Cα) (Å)
$cPLA_2$ (ref *22* and herein)*	52	53	24.3	0.3	L39	7.0
$cPLA_2$ (refs *23* and *32*)	68	66	30.5	3.1	V97	9.8
SytIA (refs *28* and *45*)	71	90	25.7	−1.2	R234	5.3
PKCα (refs *29* and *35*)	77	64	23.1	−2.6	T250	5.2

[a] A comparison of four models (including the present model*) for the docking of the $cPLA_2$, SytIA, and PKCα C2 domains to membranes. Three equivalent atoms from each structure were used to define a universal starting position in which a calibration β-strand is perpendicular to the membrane, and the entire domain lies in the aqueous phase. Figure 8 illustrates the rotations and translation used to convert this starting position into the final docking model. The first rotation (θ) is about the molecular x'-axis, which is perpendicular to the calibration β-strand and lies in the plane of the calibration β-sheet. The second rotation (φ) is about the molecular z'-axis collinear with the calibration β-strand. Finally, a translation perpendicular to the membrane (Z_{trans}) brings the C2 domain to the correct membrane penetration depth. Also shown for each model is the average depth of its multiple Ca^{2+} ions, and the depth of its most deeply buried α-carbon, relative to the headgroup phosphate plane. Angles are given in degrees, and depths are given in angstroms.

The method used to develop the refined docking model (see Results) started with the angular orientation of a specific crystal structure (PDB 1rlw) and is thus convenient for orienting this structure relative to the membrane surface. To facilitate comparisons between the docking geometries of different C2 domains, an alternative approach was developed that can be easily used to generate docking angles and depths for any membrane-bound C2 domain. In this approach, the docking angles are determined by three selected α-carbons in the same β-sheet. When the docking of different C2 domain structures is compared, the same three atoms are chosen at structurally homologous positions in the corresponding β-sheet. Here, for example, we compare docking models based on the crystal structure of the C2 domain of $cPLA_2$, the NMR structure of the C2 domain of $cPLA_2$, the crystal structure of the C2 domain of protein kinase Cα, and the NMR structure of the first C2 domain of synaptotagmin I (*32*, *35*, *45*). Two of the selected α-carbons (20 and 27 in $cPLA_2$, 173 and 180 in PKCα, 158 and 165 in SytIa) are used to define a vector representing the longest β-strand in the C2 domain, which is located at a structurally conserved position in the C2 motif. A separate, perpendicular vector is defined by the third α-carbon (118 in $cPLA_2$, 271 in PKCα, and 256 in SytIa) located in the furthest β-strand in the same sheet. The coordinate system places the molecular z'-axis along the first vector, while the x'-axis is parallel to the second vector and translated so it passes through the first α-carbon. A common starting position is defined for all domains with the z-axis normal to the membrane plane and the first atom lying 50 Å from the headgroup phosphate plane, such that there is no initial contact with the membrane. Subsequently, each domain is rotated and translated in a defined way until it reaches the final position specified by its published docking model. This transformation is described in Figure 8, which illustrates how the starting position is converted to the final position by a rotation about the molecular x'-axis, followed by a rotation about the molecular z'-axis (the β-strand), followed by a translation along the membrane normal to yield the angular orientation and depth of the final model. For the present optimized docking model of the $cPLA_2$ C2 domain, the first rotation angle is accurate to within 3°, and the second angle is accurate to within 5°, while the depth of penetration of a given backbone atom is accurate to within 1 Å, as revealed by controlled displacements from the model.

Table 3 compares the two rotations needed to generate each of the four C2 domain docking models. The first angle represents the tilt of the calibration β-strand with respect to the membrane normal (Figure 8). Comparing the two docking models of the $cPLA_2$ C2 domain (present study and ref *32*), this angle is 16° smaller for the present refined model than for the previous model, indicating that the β-strands are significantly more perpendicular to the membrane than previously proposed. Comparing the refined model of the $cPLA_2$ C2 domain with the models for the PKCα and SytIa C2 domains (present study and refs *35* and *45*), this angle ranges from 52 to 71 and 77°, respectively, indicating that the β-sheets of the latter two domains are significantly more parallel to the membrane surface than the $cPLA_2$ C2 domain. Such a parallel orientation is consistent with the proposed ionic interactions of the β-sheets in the PKCα and SytIa C2 domains with anionic headgroups on the membrane surface (*30*, *35*, *52*). The second angle (Figure 8, Table 3) is more difficult to interpret and less interesting since it is sensitive to variations in the flatness of the calibration β-sheet, making comparisons between different domains difficult.

Notably, the depths of penetration also differ between models as summarized in Table 3. The original model of $cPLA_2$ places the Ca^{2+} ions at an average position 3 Å deeper in the membrane than the headgroup phosphate layer, such that the Ca^{2+} ions penetrate the hydrocarbon core. By contrast, the present $cPLA_2$ model and the recent models for PKCα and SytIa C2 domains all place the Ca^{2+} ions in the headgroup layer. Significantly, in the improved $cPLA_2$

model, the proximity of the Ca^{2+} ions to the phosphate plane provides strong support for the existence of direct Ca^{2+} coordination by headgroup phosphate oxygens, as suggested by crystal structures of complexes between C2 domains and headgroup analogues (*29*, *30*). Such direct Ca^{2+} coordination would provide an important interaction stabilizing the protein−membrane complex. Finally, loops I and III of the refined cPLA$_2$ model penetrate significantly more deeply into the hydrocarbon core than in the PKCα and SytIa models (Table 3), consistent with the hydrophobic docking mechanism of the former C2 domain and the ionic docking mechanisms of the latter C2 domains (*3*, *16*), as well as the differences in the kinetics of membrane association and dissociation observed for these domains (*3*, *53*, *54*).

Mechanism of Ca^{2+}-Dependent Activation. Two general classes of models have been proposed for the Ca^{2+}-activation mechanism of the C2 domain of cPLA$_2$. The simplest model proposes that the domain is an electrostatic switch in which no Ca^{2+}-triggered structural changes occur: in this model, Ca^{2+} ions bind to a preformed site and alter the surface electrostatics of the protein, thereby neutralizing an electrostatic barrier to membrane docking and penetration (*55*). Other models propose that Ca^{2+} binding triggers a conformational switch in the C2 domain, yielding structural changes essential for docking. The present findings disfavor or place strong limits on the magnitude of such Ca^{2+}-triggered structural changes since the effects of Ca^{2+} on EPR probes in the Ca^{2+}-binding loops are subtle and highly localized. Instead, the results support a modified version of the electrostatic switch model in which the average conformation of the membrane docking surface does not significantly change during activation. However, the observed proximity of the bound Ca^{2+} ions to the lipid headgroup phosphates in the membrane-docked state suggests that direct coordination bonds are formed between the Ca^{2+} ions and the phosphate oxygens. Such coordination bonds are proposed to stabilize the activated state and thus contribute to activation, thereby adding a second activation mechanism to the nonspecific electrostatic interactions proposed by the electrostatic switching model.

Finally, in the full-length cPLA$_2$ enzyme, the Ca^{2+}-activated C2 domain must dock to the membrane in an orientation that allows productive docking of the catalytic domain, which hydrolyzes membrane-bound lipids, to the membrane surface nearby. The crystal structure of full-length cPLA$_2$ reveals that the C2 and catalytic domains are connected by a long, flexible linker (*24*). In the crystal, the two domains are not oriented in a way that allows them both to dock the appropriate protein surfaces to a membrane surface. However, low-energy rotations of torsion angles in the linker are sufficient to reorient (not shown) the two domains so that the C2 domain can dock to the membrane in the orientation proposed herein, while at the same time the active site of the catalytic domain is contacting the membrane surface in the appropriate orientation for its phospholipase activity. Thus, the proposed model for C2 domain docking is fully compatible with the biological function of the intact enzyme.

ACKNOWLEDGMENT

We thank Drs. James Clark and Eric Nalefski for originally making available the expression system for cPLA$_2$; Dr. Eric Nalefski and Mark Wisner for engineering some of the cysteine mutants utilized; and Drs. David Cafiso, April Frazier, Susy Kohout, and Eric Nalefski for helpful discussions.

REFERENCES

1. Rotin, D., Staub, O., and Haguenauer-Tsapis, R. (2000) *J. Membr. Biol. 176*, 1−17.
2. Tomsig, J. L., and Creutz, C. E. (2002) *Cell Mol. Life Sci. 59*, 1467−77.
3. Nalefski, E. A., Wisner, M. A., Chen, J. Z., Sprang, S. R., Fukuda, M., Mikoshiba, K., and Falke, J. J. (2001) *Biochemistry 40*, 3089−100.
4. Nalefski, E. A., and Falke, J. J. (1996) *Protein Sci. 5*, 2375−90.
5. Cho, W. (2001) *J. Biol. Chem. 276*, 32407−10.
6. Rizo, J., and Sudhof, T. C. (1998) *J. Biol. Chem. 273*, 15879−82.
7. Kohout, S. C., Corbalan-Garcia, S., Torrecillas, A., Gomez-Fernandez, J. C., and Falke, J. J. (2002) *Biochemistry 41*, 11411−24.
8. Hurley, J. H., and Meyer, T. (2001) *Curr. Opin. Cell Biol. 13*, 146−52.
9. Hurley, J. H., and Misra, S. (2000) *Annu. Rev. Biophys. Biomol. Struct. 29*, 49−79.
10. Hurley, J. H., Tsujishita, Y., and Pearson, M. A. (2000) *Curr. Opin. Struct. Biol. 10*, 737−43.
11. Edwards, A. S., and Newton, A. C. (1997) *Biochemistry 36*, 15615−23.
12. Farber, S. A., Olson, E. S., Clark, J. D., and Halpern, M. E. (1999) *J. Biol. Chem. 274*, 19338−46.
13. Nalefski, E. A., Sultzman, L. A., Martin, D. M., Kriz, R. W., Towler, P. S., Knopf, J. L., and Clark, J. D. (1994) *J. Biol. Chem. 269*, 18239−49.
14. Clark, J. D., Schievella, A. R., Nalefski, E. A., and Lin, L. L. (1995) *J. Lipid Mediat. Cell Signal 12*, 83−117.
15. Hegen, M., Sun, L., Uozumi, N., Kume, K., Goad, M. E., Nickerson-Nutter, C. L., Shimizu, T., and Clark, J. D. (2003) *J. Exp. Med. 197*, 1297−302.
16. Davletov, B., Perisic, O., and Williams, R. L. (1998) *J. Biol. Chem. 273*, 19093−6.
17. Ananthanarayanan, B., Das, S., Rhee, S. G., Murray, D., and Cho, W. (2002) *J. Biol. Chem. 277*, 3568−75.
18. Zhang, X., Rizo, J., and Sudhof, T. C. (1998) *Biochemistry 37*, 12395−403.
19. Nalefski, E. A., Slazas, M. M., and Falke, J. J. (1997) *Biochemistry 36*, 12011−8.
20. Fernandez-Chacon, R., Shin, O. H., Konigstorfer, A., Matos, M. F., Meyer, A. C., Garcia, J., Gerber, S. H., Rizo, J., Sudhof, T. C., and Rosenmund, C. (2002) *J. Neurosci. 22*, 8438−46.
21. Kulkarni, S., Das, S., Funk, C. D., Murray, D., and Cho, W. (2002) *J. Biol. Chem. 277*, 13167−74.
22. Perisic, O., Fong, S., Lynch, D. E., Bycroft, M., and Williams, R. L. (1998) *J. Biol. Chem. 273*, 1596−604.
23. Xu, G. Y., McDonagh, T., Yu, H. A., Nalefski, E. A., Clark, J. D., and Cumming, D. A. (1998) *J. Mol. Biol. 280*, 485−500.
24. Dessen, A., Tang, J., Schmidt, H., Stahl, M., Clark, J. D., Seehra, J., and Somers, W. S. (1999) *Cell 97*, 349−60.
25. Sutton, R. B., and Sprang, S. R. (1998) *Structure 6*, 1395−405.
26. Sutton, R. B., Davletov, B. A., Berghuis, A. M., Sudhof, T. C., and Sprang, S. R. (1995) *Cell 80*, 929−38.
27. Essen, L. O., Perisic, O., Lynch, D. E., Katan, M., and Williams, R. L. (1997) *Biochemistry 36*, 2753−62.
28. Shao, X., Fernandez, I., Sudhof, T. C., and Rizo, J. (1998) *Biochemistry 37*, 16106−15.
29. Verdaguer, N., Corbalan-Garcia, S., Ochoa, W. F., Fita, I., and Gomez-Fernandez, J. C. (1999) *EMBO J. 18*, 6329−38.
30. Ochoa, W. F., Corbalan-Garcia, S., Eritja, R., Rodriguez-Alfaro, J. A., Gomez-Fernandez, J. C., Fita, I., and Verdaguer, N. (2002) *J. Mol. Biol. 320*, 277−91.
31. Nalefski, E. A., and Falke, J. J. (1998) *Biochemistry 37*, 17642−50.
32. Frazier, A. A., Wisner, M. A., Malmberg, N. J., Victor, K. G., Fanucci, G. E., Nalefski, E. A., Falke, J. J., and Cafiso, D. S. (2002) *Biochemistry 41*, 6282−92.
33. Gerber, S. H., Rizo, J., and Sudhof, T. C. (2001) *J. Biol. Chem. 276*, 32288−92.

34. Chapman, E. R., and Davis, A. F. (1998) *J. Biol. Chem. 273*, 13995−4001.
35. Kohout, S. C., Corbalan-Garcia, S., Gomez-Fernandez, J. C., and Falke, J. J. (2003) *Biochemistry 42*, 1254−65.
36. Altenbach, C., Flitsch, S. L., Khorana, H. G., and Hubbell, W. L. (1989) *Biochemistry 28*, 7806−12.
37. Kunkel, T. A., Roberts, J. D., and Zakour, R. A. (1987) *Methods Enzymol. 154*, 367−82.
38. Nalefski, E. A., and Falke, J. J. (2002) *Methods Mol. Biol. 172*, 295−303.
39. Hubbell, W. L., Cafiso, D. S., and Altenbach, C. (2000) *Nat. Struct. Biol. 7*, 735−9.
40. Columbus, L., and Hubbell, W. L. (2002) *Trends Biochem. Sci. 27*, 288−95.
41. Altenbach, C., Greenhalgh, D. A., Khorana, H. G., and Hubbell, W. L. (1994) *Proc. Natl. Acad. Sci. U.S.A. 91*, 1667−71.
42. Taylor, J. R. (1997) *An Introduction to Error Analysis*, 2nd ed., University Science Books, Sausalito, CA.
43. Langen, R., Oh, K. J., Cascio, D., and Hubbell, W. L. (2000) *Biochemistry 39*, 8396−405.
44. Ellena, J. F., Archer, S. J., Dominey, R. N., Hill, B. D., and Cafiso, D. S. (1988) *Biochim. Biophys. Acta 940*, 63−70.
45. Frazier, A. A., Roller, C. R., Havelka, J. J., Hinderliter, A., and Cafiso, D. S. (2003) *Biochemistry 42*, 96−105.
46. Dalton, L. A., McIntyre, J. O., and Fleischer, S. (1987) *Biochemistry 26*, 2117−30.
47. Ramachandran, G. N., and Sasisekharan, V. (1968) *Adv. Protein Chem. 23*, 283−438.
48. Lichtenbergova, L., Yoon, E. T., and Cho, W. (1998) *Biochemistry 37*, 14128−36.
49. Perisic, O., Paterson, H. F., Mosedale, G., Lara-Gonzalez, S., and Williams, R. L. (1999) *J. Biol. Chem. 274*, 14979−87.
50. Bittova, L., Sumandea, M., and Cho, W. (1999) *J. Biol. Chem. 274*, 9665−72.
51. Gerber, S. H., Rizo, J., and Sudhof, T. C. (2002) *Diabetes 51 Suppl. 1*, S12−8.
52. Corbalan-Garcia, S., Garcia-Garcia, J., Rodriguez-Alfaro, J. A., and Gomez-Fernandez, J. C. (2003) *J. Biol. Chem. 278*, 4972−80.
53. Nalefski, E. A., and Newton, A. C. (2001) *Biochemistry 40*, 13216−29.
54. Stahelin, R. V., and Cho, W. (2001) *Biochemistry 40*, 4672−8.
55. Murray, D., and Honig, B. (2002) *Mol. Cell 9*, 145−54.
56. Kraulis, P. J. (1991) *J. Appl. Crystallogr. 24*, 946−50.
57. Fanucci, G. E., Cadieux, N., Piedmont, C. A., Kadner, R. J., and Cafiso, D. S. (2002) *Biochemistry 41*, 11543−51.
58. Ball, A., Nielsen, R., Gelb, M. H., and Robinson, B. H. (1999) *Proc. Natl. Acad. Sci. U.S.A. 96*, 6637−42.
59. Heller, H., Schaefer, M., and Schulten, K. (1993) *J. Phys. Chem. 97*, 8343−60.
60. Heller, H., Schaefer, M., and Schulten, K. (1993) *J. Phys. Chem. 97*, 8343−8360.

BI035119+